

Piecewise assembled acoustic arrays based on reconfigurable tessellated structures

Chengzhe Zou, and Ryan L. Harne

Citation: [The Journal of the Acoustical Society of America](#) **144**, 2324 (2018); doi: 10.1121/1.5064281

View online: <https://doi.org/10.1121/1.5064281>

View Table of Contents: <http://asa.scitation.org/toc/jas/144/4>

Published by the [Acoustical Society of America](#)

Piecewise assembled acoustic arrays based on reconfigurable tessellated structures

Chengzhe Zou and Ryan L. Harné^{a)}

Department of Mechanical and Aerospace Engineering, The Ohio State University, Columbus, Ohio 43210, USA

(Received 12 March 2018; revised 6 August 2018; accepted 27 September 2018; published online 22 October 2018)

Physically reconfigurable, tessellated acoustic arrays inspired by origami structures have recently been leveraged to adaptively guide acoustic energy. Yet, the prior work only examined tessellated arrays composed from uniform folding patterns, so that the limited folding-induced shape change prohibits broad acoustic field tailoring. To explore a wider range of opportunities by origami-inspired acoustic arrays, here, piecewise geometries are assembled from multiple folding patterns so that acoustic transducer elements are reconfigured in more intricate ways upon array folding. An analytical model of assembled geometries and resulting acoustic wave radiation from the oscillating facets is formulated. Using the theoretical tool, parametric investigations are undertaken to study the adaptation of acoustic energy transmission caused by folding and modularity of the array assembly. A proof-of-concept specimen is fabricated and experiments are conducted to validate the theoretical model and to investigate the efficacy of the piecewise acoustic array concept. The total findings reveal that the assembly of tessellated acoustic arrays may emulate the wave radiation emitted by ideal acoustic sources of intricate shapes. Moreover, by exploitation of origami folding actions, the shape adaptations of the proposed arrays permit straightforward wave guiding opportunities for diverse application needs. © 2018 Acoustical Society of America.

<https://doi.org/10.1121/1.5064281>

[MDV]

Pages: 2324–2333

I. INTRODUCTION

Recently, origami-inspired reconfigurable arrays for wave guiding have been investigated in many applied sciences and engineering fields. The properties of the arrays are governed by the mechanical configurations, which control the wave interference behaviors whether for transmitted wave radiation or received wave signals. For example, real-time adaptation of system properties is achieved for reconfigurable radio frequency antennas,^{1,2} tunable wave propagation guides,^{3,4} and optical lenses,^{5,6} to name a few. By leveraging low-dimensional origami structures, folding-induced geometric shape change is able to adaptively tailor the characteristics of these arrays according to application demands.

Arrays of acoustic elements, whether transmitters or receivers, are also commonly employed to guide acoustic energy delivery and reception.^{7,8} Acoustic arrays are conventionally controlled by time delays and amplitude weights for each transducer element.^{9,10} These digital interventions play the role to virtually reposition transducer elements so as to adjust interference effects although the transducers remain physically fixed in space. Yet, this digital technique⁹ is typically accompanied by computational burden and complex implementation. This is because a sufficiently large number of transducer elements is required for effective wave guiding, while each element needs independent control so as to impede straightforward implementation. Such challenges

occur for acoustic arrays in ultrasound surgery,¹¹ non-destructive evaluation,¹² and underwater monitoring,¹³ among others.

To provide similar adaptive control functionality without such disadvantages, one idea may be to employ mechanically reconfigurable arrays of acoustic transducer elements in the spirit of the undertakings in electromagnetics^{1,2} and optics.^{5,6} Established upon an origami-inspired folding pattern, the facets are considered to be ideal vibrating, baffled pistons that radiate acoustic waves, as shown in Fig. 1(b) for a transmitter type of array. When the shape of the array is reconfigured via simple low-dimensional folding, the transducers are physically redistributed causing change in acoustic energy delivery.^{14,15} In this concept, one driving signal is sent to all of the transducers. Consequently, the wave interference effects are controlled by the folding-induced repositioning of transducer elements. As such, challenges of computation and implementation are lessened or avoided altogether. Prior results also revealed that tessellated arrays enable acoustic wave guiding capability better than digitally controlled arrays using fewer or an equal number of transducer elements.¹⁶ Moreover, the low dimensionality and foldability of origami cultivate unique portability.^{17,18} One may envision such advantages of system compactness and deployability for unique applications of acoustic arrays such as sonar¹⁹ or ultrasound wave guiding.²⁰

The use of origami tessellations introduces further advantages for acoustic array practices when compared to other mechanical methods for reconfiguration like bending a surface with continuously distributed acoustic elements.²¹

^{a)}Electronic mail: harné.3@osu.edu

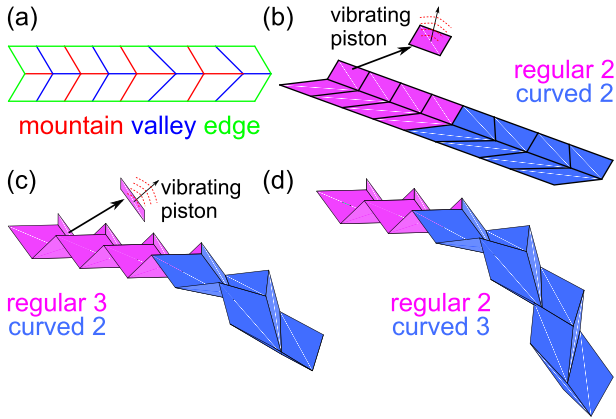


FIG. 1. (Color online) Overview of assembly of Miura-ori-based tessellations. (a) Crease pattern of piecewise geometry assembled from two regular and two curved Miura-ori unit cells. (b) Piecewise, unfolded geometry of two regular and two curved Miura-ori unit cells. (c) Piecewise geometry of three regular and two curved Miura-ori unit cells under folded state. (d) Piecewise geometry of two regular and three curved Miura-ori unit cells under the same folding extent of (c).

Due to low-dimensionality in kinematic and/or mechanical behavior, origami tessellations undergo large shape changes with few folding actions, enabling enhanced repeatability of achieving desired conformations^{22,23} when compared to bending a surface.

Despite the knowledge made on foldable, tessellated acoustic arrays, the tessellated acoustic transducer arrays studied to date^{14–16} are only composed of one folding pattern. Consequently, the folding-induced topological changes are limited. A diverse set of operating requirements for a guided wave device may demand a broader range of physical conformations.²⁴ For example, Ureda²⁵ and Keele²⁶ investigated acoustic line arrays of various shapes to adjust acoustic wave propagation. Among them, the J-shaped line array is an example that would not be achieved by a single folding pattern since the J-shape is a combination of a straight line and an arc.

To advance understanding of foldable acoustic arrays, in this research multiple folding patterns are assembled to construct piecewise tessellated acoustic transducer arrays. By the integration of modular array elements with different folding patterns, the modularity of the system permits a broad range of array reconfiguration due to the distinct topological change of different modules. To demonstrate the idea, this research gives attention to the J-shaped line array since it has broad relevance for acoustic communication applications.²⁵ To realize folding patterns that may be assembled in a piecewise manner, derivatives of the Miura-ori folding pattern explored by Gattas *et al.*^{27,28} are employed here due to the compatibility of the derivatives to be assembled together. Although the J-shaped array is studied in this report, origami patterns may be designed to adopt nearly arbitrary conformations when folded,^{22,23} which suggests broad versatility for tailoring acoustic properties via origami-inspired acoustic arrays.

To illustrate the modular array idea, one folding pattern composed of regular and curved Miura-ori parts is shown in Fig. 1(a). The corresponding unfolded tessellation is

illustrated in Fig. 1(b) in an isometric view. Once the tessellated array is folded, the regular Miura-ori emulates the straight part of the J-shaped line array while the curved Miura-ori part contributes to the curved, arc-like segment, as shown in Fig. 1(c) in a partially folded form. The configuration of the piecewise assembled array can be adjusted by the folding extent and the modularity of the array assembly. Comparing the piecewise tessellations in Figs. 1(c) and 1(d) with different numbers of modules, the distinctions of geometric shapes are evident although the folding extent is the same. The array shown in Fig. 1(c) includes three and two unit cells of regular and curved Miura-ori, respectively, whereas the array in Fig. 1(d) is assembled from two and three unit cells of regular and curved Miura-ori, respectively. This exemplifies that the assembly of modular, foldable acoustic array components may enable broad tailoring of the resulting acoustic field.

This research aims to establish and explore the concept of foldable, tessellated acoustic arrays assembled from piecewise, modular unit cells. To undertake the effort, this report is organized as follows. Section II presents an analytical model to characterize the acoustic field radiated from piecewise assembled folding acoustic elements. Then, investigations are undertaken to explore the capability of piecewise, tessellated arrays to adaptively guide acoustic energy. An experimental validation of the analysis is conducted using a proof-of-concept specimen to test the practical efficacy of the concept. Finally, the new findings are summarized with concluding discussion.

II. ANALYTICAL MODEL FORMULATION

To evaluate the acoustic wave guiding properties of the piecewise acoustic transducer array, an analytical model is developed to predict the radiated acoustic pressure due to the oscillating, tessellated facets. This section first describes the geometry of the Miura-ori-based tessellations and the piecewise assembly. Then Rayleigh's integral is employed to characterize the acoustic energy delivery as the superposition of contributions from all the oscillating facets.

The geometries of the regular and curved Miura-ori sub-arrays are established separately. Then, the sub-arrays are assembled together to form the piecewise array. A folded unit cell of regular Miura-ori is shown in Fig. 2(a). The vertices of the same color stay on the same plane during folding. The topology of the unit cell in Fig. 2(a) is determined by edge lengths a and b , edge angle γ , and folding angle θ . Alternatively, its folded shape is described by the spatial extents H , S , L , and V whose expressions are derived in Ref. 29 and briefly summarized in the Appendix of this work. The coordinates of vertices can be expressed via these folding extents conveniently, e.g., the location of point 1 in Fig. 2(a) is

$$[x_1, y_1, z_1] = [S, -L - V, -H], \quad (1)$$

where $[x_i, y_i, z_i]$ refers to the x , y , and z coordinates of the i th vertex.

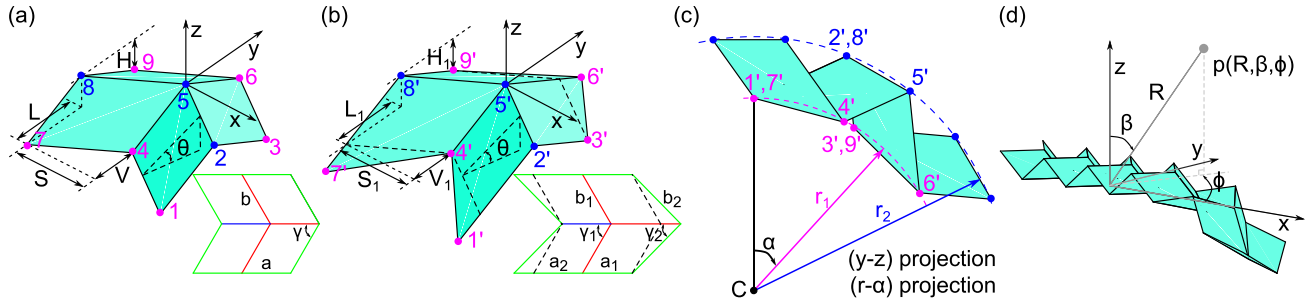


FIG. 2. (Color online) (a) Geometrical notations to define folded unit cell of regular Miura-ori and its crease pattern. (b) Geometrical notations to define folded unit cell of curved Miura-ori and its crease pattern. (c) Schematic presenting the curvature of curved Miura-ori array in which the colored vertices lie on the cylindrical surface of the corresponding color. C and r refer to circle center and radius, respectively. (d) Analytical model notation to predict the sound pressure radiated from the piecewise, tessellated source to the field point $p(R, \beta, \phi)$.

Then for the sub-array of regular Miura-ori, the coordinates of point 1 in the (m, n) unit cell are

$$\begin{aligned} [x_{1(m,n)}, y_{1(m,n)}, z_{1(m,n)}] \\ = [S + 2(m-1)S, -L - V + 2(n-1)L, -H], \end{aligned} \quad (2)$$

where m and n refer to the numbering of the unit cell of regular Miura-ori in x and y dimensions, respectively.

In terms of curved Miura-ori presented in Fig. 2(b), a greater number of parameters define its folding pattern because the mountain creases are not parallel with valley creases. Seven parameters, including edge lengths a_1 , a_2 , b_1 , and b_2 , edge angles γ_1 and γ_2 , and folding angle θ are illustrated in Fig. 2(b). Among them, five parameters are independent²⁷ since

$$b_1 \sin(\gamma_1) = b_2 \sin(\gamma_2), \quad (3a)$$

$$a_1 + b_2 \cos(\gamma_2) = a_2 + b_1 \cos(\gamma_1). \quad (3b)$$

For the unit cell of curved Miura-ori, the vertices of the same color in Figs. 2(b) and 2(c) reside on the same cylindrical surface when folded. Therefore, the arc center and radii

must be determined to model the folded topology of the sub-array of curved Miura-ori. The two cylindrical surfaces delineated by the two arcs, shown as dashed curves in Fig. 2(c), are concentric.²⁷

As indicated by the dashed profile in Fig. 2(b), the curved Miura-ori unit cell includes a regular Miura-ori defined by a_1 , b_1 , and γ_1 . Both unit cells share vertices, except for points $1'$, $6'$, and $7'$ that are unique to the curved Miura-ori. The coordinates of the unshared vertices are tailored based on linear proportionality. Considering point $1'$, for instance,

$$[x_{1'}, y_{1'}, z_{1'}] = \left[S_1, -\frac{a_2}{a_1}L_1 - V_1, -\frac{a_2}{a_1}H_1 \right] \quad (4)$$

where H_1 , S_1 , L_1 , and V_1 are the spatial extents of the included unit cell of regular Miura-ori.

For linear assemblies of unit cells of curved Miura-ori, the cylindrical surface revolves around the x axis. Hence, the coordinates of the vertices are expressed in a cylindrical coordinate system (x, r, α) . The radii of two circles are obtained by determining the arc center C in the Cartesian coordinate system in Fig. 2(b), and the y and z coordinates of the center are

$$y_C = \frac{y_{1'}^2(z_{4'} - z_{3'}) + y_{3'}^2(z_{1'} - z_{4'}) + y_{4'}^2(z_{3'} - z_{1'}) + (z_{1'} - z_{4'})(z_{1'} - z_{3'})(z_{4'} - z_{3'})}{2[y_{1'}(z_{4'} - z_{3'}) + y_{3'}(z_{1'} - z_{4'}) + y_{4'}(z_{3'} - z_{1'})]}, \quad (5a)$$

$$z_C = \frac{y_{1'}(y_{4'}^2 - y_{3'}^2 + z_{4'}^2 - z_{3'}^2) + y_{3'}(y_{1'}^2 - y_{4'}^2 + z_{1'}^2 - z_{4'}^2) + y_{4'}(y_{3'}^2 - y_{1'}^2 - z_{1'}^2 + z_{3'}^2)}{2[y_{1'}(z_{4'} - z_{3'}) + y_{3'}(z_{1'} - z_{4'}) + y_{4'}(z_{3'} - z_{1'})]}. \quad (5b)$$

Therefore, the radii of these two arcs in Fig. 2(c) are, respectively,

$$r_1 = \sqrt{(y_3 - y_C)^2 + (z_3 - z_C)^2}, \quad (6a)$$

$$r_2 = \sqrt{(y_2 - y_C)^2 + (z_2 - z_C)^2}. \quad (6b)$$

The location of point $1'$ in the cylindrical coordinate system is thus

$$[x_{1'}, r_{1'}, \alpha_{1'}] = [S_1, r_1, 0]. \quad (7)$$

For the sub-array of curved Miura-ori, the coordinates of point $1'$ in the (m', n') unit cell are

$$\begin{aligned} [x_{1'(m',n')}, r_{1'(m',n')}, \alpha_{1'(m',n')}] \\ = [S_1 + 2(m'-1)S_1, r_1, 0 + 2(n'-1)A], \end{aligned} \quad (8)$$

where m' and n' refer to the numbering of the unit cell of curved Miura-ori in x and α dimensions, respectively. The

periodicity of the curved Miura-ori array in the α dimension is A , and it is the radius angle of the chord connected by point 1' and point 6' in Fig. 2(b),

$$\sin \frac{1}{2}A = \frac{\sqrt{(y_{1'} - y_{6'})^2 + (z_{1'} - z_{6'})^2}}{2r_1}. \quad (9)$$

With the geometric models of sub-arrays of regular and curved Miura-ori, the piecewise tessellated array is assembled by the compatibility of shared vertices. Specifically, by making points 2, 5, and 8 in a regular Miura-ori sub-array [Fig. 2(a)] coincident with points 2', 5', and 8' in a curved Miura-ori sub-array [Fig. 2(b)], geometric compatibility is achieved.^{27,28} The piecewise crease pattern and tessellation are shown in Fig. 1. As a result, the parameters of a regular Miura-ori sub-array a , b , and γ are the same as a_1 , b_1 , and γ_1 for the adjacent curved Miura-ori sub-array. The folding angle θ is defined the same for both patterns.

To characterize the J-shape of the piecewise source, the length of the straight line and the covered radius angle of the arc segment are defined as

$$L_{\text{line}} = 2NL, \quad (10a)$$

$$A_{\text{arc}} = N'A, \quad (10b)$$

where N is the number of unit cells in the y dimension of the sub-array of regular Miura-ori, and N' is the number of unit cells in the α dimension of the sub-array of curved Miura-ori.

Based on the geometry of the piecewise array, Rayleigh's integral is employed to characterize the acoustic waves radiated from the facets. Each facet is assumed to be mounted in an infinite rigid baffle and assumed to then oscillate normally to that baffle. The field point location is defined by the radial distance R , elevation angle β , and azimuth angle ϕ , as shown in Fig. 2(d). By Rayleigh's integral and linear superposition, the radiated acoustic pressure delivered from all of the baffled facets is

$$p(R, \beta, \phi, t) = j \frac{\rho_0 \omega u_0}{2\pi} e^{j\omega t} \sum_{i=1}^M \left\{ \int_{A_i} \frac{e^{-jkR_i}}{R_i} dA_i \right\}, \quad (11)$$

where the density of the fluid medium is ρ_0 ; ω is the angular frequency of the time-harmonic oscillation of each facet; A_i is the area of the i th surface; u_0 is the amplitude of the uniform, normal velocity over A_i ; $k = \omega/c_0$ is the acoustic wavenumber with the sound speed c_0 ; R_i is the distance from the field point to the center of the i th area; and M is the number of areas. In this work, $\rho_0 = 1.21 \text{ kg/m}^3$ and $c_0 = 343 \text{ m/s}$ (Ref. 7) are used for all computations.

Since the facets are assumed to be individually baffled, the radiated acoustic waves cannot propagate to field points that are beneath the baffled plane of each facet. Thus, computation of Rayleigh's integral over each facet is taken according to the satisfaction of the constraint

$$0 \leq \beta_i \leq \pi/2, \quad (12)$$

where β_i is the local elevation angle for the i th tessellated facet.

To guarantee the accuracy of the prediction from Eq. (11), convergence studies are undertaken via the approach developed by Ocheltree and Frizzell.³⁰ By the approach, a vibrating panel is discretized into a mesh of smaller elements. With continued mesh refinement, the dimensions of the discretized sources become sufficiently small such that they are point sources distributed over the panel plane with respect to a distant field point. This research uses such an approach to densely refine a mesh created from the tessellated facets of piecewise Miura-ori-based acoustic array. The mesh refinement described above permits the simplification of Eq. (11) to

$$p(R, \beta, \phi, t) = j \frac{\rho_0 \omega u_0}{2\pi} e^{j\omega t} \sum_{i=1}^M \left\{ \frac{e^{-jkR_i}}{R_i} A_i \right\}. \quad (13)$$

Equation (13) may be rapidly computed and is sufficiently accurate so long as a convergence of results is obtained by superior discretization routines, such as is undertaken in this research. Finally, the sound pressure level (SPL) is computed by

$$\text{SPL} = 20 \log_{10} \left[\frac{p_{\text{rms}}(R, \beta, \phi)}{p_{\text{ref}}} \right], \quad (14)$$

where the subscript "rms" is the root-mean-square value of $p(R, \beta, \phi)$ and $p_{\text{ref}} = 20 \text{ } \mu\text{Pa}$. The SPL is utilized in the evaluation of the adaptive acoustic wave radiation delivered from piecewise acoustic arrays.

III. STUDIES AND DISCUSSIONS

In this section, the analytical model developed in Sec. II is leveraged to assess the potential of piecewise, foldable, and tessellated acoustic arrays to emulate the wave guiding characteristics of the conventional J-shaped acoustic array. Through such investigations, the adaptation of acoustic fields enabled by the proposed folding and modular acoustic arrays is scrutinized.

A. Influence of tessellation refinement on the far field wave radiation

As shown in Figs. 1(c) and 1(d), the piecewise assembled acoustic arrays approximate an ideal J-shaped acoustic source widely used for communication systems. To better approximate the shape, the tessellated array may be refined by a greater density of unit cells while the overall array size remains unchanged. The refinement of the tessellated array is shown in the insets of Fig. 3 along with the contrast to the ideal J-shaped source. With array refinement, the unit cell dimensions and the required folding extent to achieve the overall J-shape are decreased. Consequently the folding-induced variation of the origami surface is reduced, and the accuracy of the approximation with the ideal J-shape is improved. Hereafter, the comparisons of the tessellated arrays are made to the conventional J-shaped line array that is referred to as the "ideal source."

The influence of tessellation refinement on the resulting acoustic field is presented in Fig. 3 at a radial distance that is sufficiently large, $R = 20 \text{ m}$, so that far field wave radiation

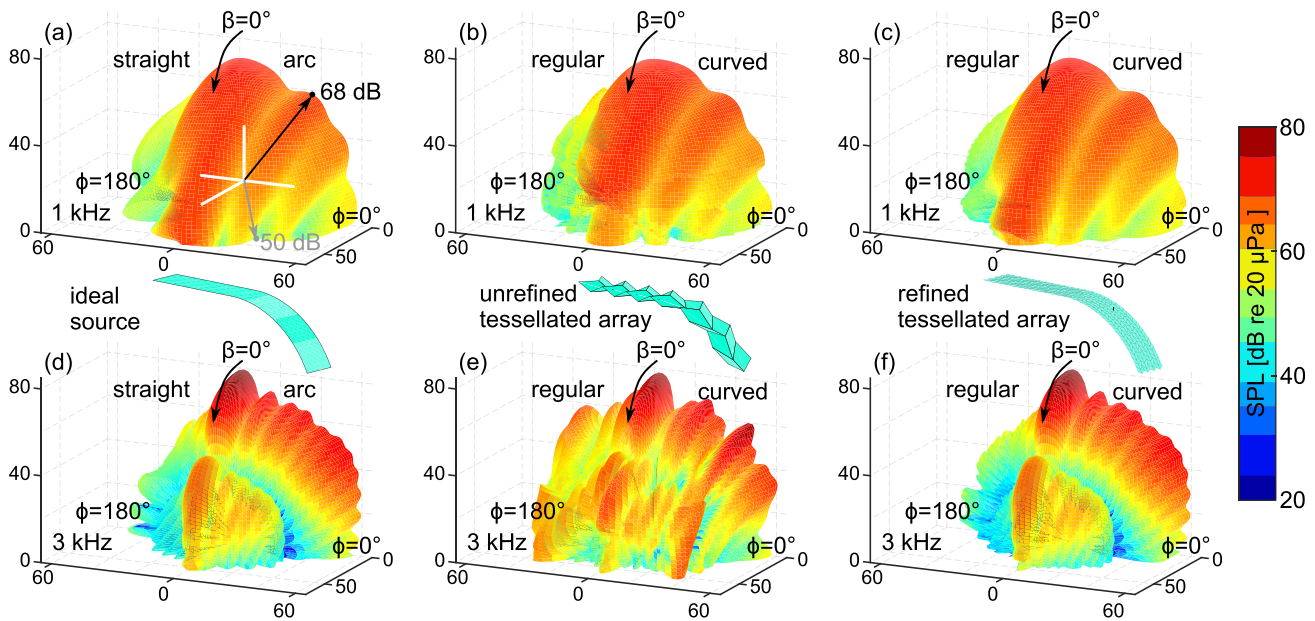


FIG. 3. (Color online) SPL of acoustic sources as a function of the elevation angle β and azimuth angle ϕ of the far field point at R is 20 m. The color and the radial distance from the origin indicate the magnitude of the SPL, which is exemplified by two field points in (a). The acoustic sources are ideal source [(a),(d)], unrefined tessellated array [(b),(e)], and refined tessellated array [(c),(f)], respectively. Driving frequencies are 1 kHz (top row) and 3 kHz (bottom row), respectively.

is fully developed. The elevation angle β and azimuth angle ϕ ranges are $[0^\circ, 90^\circ]$ and $[0, 180^\circ]$, respectively. In Fig. 3, the color and the radial distance from the origin both indicate the magnitude of the SPL. This convention is exemplified by two example field points in Fig. 3(a), in which 50 and 68 dB of SPL are achieved at two different locations that are both 20 m away from the array.

For the unrefined array composition depicted in the middle inset of Fig. 3, the sub-arrays of regular and curved Miura-ori are both 3×1 . The folding pattern uses dimensions $a_1 = 0.105$ m, $b_1 = 0.123$ m, $\gamma_1 = 60^\circ$, and $\gamma_2 = 45^\circ$ and is folded to $\theta = 30^\circ$. In the right inset of Fig. 3, both sub-arrays are refined to 12×4 so that the unit cell dimensions and folding angle are scaled by one-fourth of the unrefined case. Thus, the refined tessellated array is folded to $\theta = 7.5^\circ$. The total oscillating surface area is the same among the three arrays. The normal surface velocity u_0 is 0.1 m/s for all arrays.

Considering the ideal source driven at 1 kHz in Fig. 3(a), it is observed that the SPL reaches a maximum at the broadside ($\beta = 0^\circ$), which is anticipated for acoustic line sources.⁷ As the field point moves away from the broadside $\beta \rightarrow 90^\circ$ to the straight side of the array along $\phi = 180^\circ$, the SPL drops significantly and the depths of nodes of SPL are more than 25 dB. The term “node” refers to the SPL reduction compared with the broadside. In contrast, the SPL is more uniform in the angular directions associated with the arc portion of the ideal source along $\phi = 0^\circ$. Based on principles of geometric acoustics,³¹ the curved portion of the ideal source is able to deliver acoustic energy more uniformly to the covered angular range, while the straight segment of the ideal source primarily contributes to the major lobe at the broadside. Viewing the top row of Fig. 3 from left to right, the directive responses of unrefined and refined tessellations are comparable to the ideal source, qualitatively and

quantitatively. This indicates that for a relatively low frequency of 1 kHz, both foldable, tessellated arrays are able to emulate the ideal acoustic source with J-shape.

Yet, at the higher driving frequency of 3 kHz, the similarities with the ideal source are suppressed for the unrefined tessellated array. For the ideal source in Fig. 3(d), the SPL has small sidelobes as $\beta \rightarrow 90^\circ$ along $\phi = 180^\circ$ and mostly uniform response along $\phi = 0^\circ$. On the other hand, the unrefined tessellation in Fig. 3(e) exhibits large fluctuation of SPL and clear evidence of sidelobes along the azimuthal plane $\phi = 180^\circ$. Although the geometric distinctions between the unrefined tessellated array and the J-shaped source are the same in Figs. 3(b) and 3(e), the phase deviations are increased with the increase of acoustic wavenumber at 3 kHz in Fig. 3(e). Such differences in the acoustic wave radiation are lessened by the array refinement in Fig. 3(f), in which the refined array recovers the trends of acoustic wave radiation as the ideal source in Fig. 3(d). Yet, the extent of array refinement preferable to deliver wave radiation comparable to the ideal source remains to be uncovered.

To bring the physics to light, the influences of refinement on the phase deviations that govern the amplitude of acoustic pressure at the field point are studied. In the computations, the ideal source is discretized into the same elements as the respective tessellated array, i.e., each discretized element within the ideal source has a counterpart in the tessellated array. The phase deviations at the field point are then computed between the ideal and tessellated array counterparts, respectively. The mean value and standard deviation of the phase deviations from all the contributing elements are considered for assessment. The phase discrepancies at the broadside $\beta = 0^\circ$ field point at $R = 20$ m are considered in this example. For this field point, the phase deviation between the unrefined tessellated array and the ideal source at 3 kHz is $81.21^\circ \pm 36.47^\circ$. In comparison, the phase

deviation between the refined tessellated array and the ideal source at 3 kHz is $23.15^\circ \pm 7.51^\circ$. In this example, the refinement of the tessellated array by four times reduces the mean error of phase reconstruction by 3.5 times. From additional parametric studies carried out (but not presented here for brevity sake), the maximum phase deviation should be approximately less than 45° for qualitative agreement between the wave fields of tessellated arrays and the ideal source. While one case of many, this study exemplifies that the refinement of the tessellated array indeed permits a good approximation of the acoustic wave radiation capability of the ideal J-shaped source.

B. Refinement of tessellated acoustic arrays for near field wave propagation control

The radiated SPL of the piecewise tessellated acoustic array in Fig. 3 is examined in the far field. To obtain insight on the origins of the development of interference effects, the acoustic fields of the ideal source and tessellated arrays are computed in a near field and transition region. The $x-z$ plane is examined and the results of SPL are presented in Fig. 4 in terms of the field point location in the plane. The distance ranges are $[-3,3]$ m and $[0,10]$ m for the x and z dimensions, respectively. The sources are baffled so that acoustic waves are not delivered to the unshaded areas in Fig. 4.

In terms of the ideal source under 1 kHz excitation in Fig. 4(a), the near field acoustic pressure is superposed by two segments corresponding to the straight and curved segments of the J-shaped source.²⁵ The straight segment accounts for the long throw of acoustic energy to the broadside³¹ as seen in Fig. 4(a) at 1 kHz and Fig. 4(d) at 3 kHz. The arc segment radiates sound in a diffused way to the directions normal to the curved oscillating surface. This contributes to a more uniform distribution of acoustic energy in the regions “below” the ideal source according to the orientations shown in Figs. 4(a) and 4(d). Considering the unrefined tessellated array in Fig. 4(b) folded to $\theta = 30^\circ$, the

acoustic field at 1 kHz is qualitatively similar to the field generated by the ideal source in Fig. 4(a). On the other hand, more pronounced sidelobes appear for the unrefined tessellated array at locations with negative x field locations in Fig. 4(b). The deviation is because certain facets are oriented to these field locations via folding. This explanation is more dramatically borne out for the case of 3 kHz wave radiation shown in Fig. 4(e) where sidelobe levels increase in the negative x locations in disagreement with the ideal source wave radiation.

With the refinement of the piecewise tessellated array while retaining the same global J-shape, a greater topological similarity is achieved between the refined tessellated array and the ideal source. Thus, at both 1 kHz and 3 kHz, the refined tessellated array exhibits a wave energy distribution in closer comparison to the ideal source as shown contrasting Figs. 4(c) to 4(a) and 4(f) to 4(d). Together, the results of Figs. 3 and 4 reveal that near and far field wave radiation of the piecewise tessellated arrays can approach the trends of acoustic energy delivered by the ideal source by the sufficient refinement of the tessellated array structure.

C. Tailoring acoustic wave propagation spectral uniformity by modularity of tessellated arrays

For piecewise tessellated arrays, the modularity may be leveraged to adjust geometric shapes for the same extent of array folding, as exemplified in Figs. 1(c) and 1(d). To study such modularity more closely, Fig. 5 presents results of far field SPL ($R = 20$ m) as a function of frequency for three different array compositions folded to the same extent. In each sub-figure of Fig. 5, six elevation angles are considered in the azimuthal plane $\phi = 0^\circ$. In Fig. 5, the size of the regular Miura-ori sub-array is 12×4 . For Figs. 5(a), 5(b), and 5(c), the sizes of the curved Miura-ori sub-arrays are, respectively, 4×4 , 8×4 , and 12×4 . Other geometric parameters pertaining to the folding pattern are the same as the refined tessellated array studied in Secs. III A and III B.

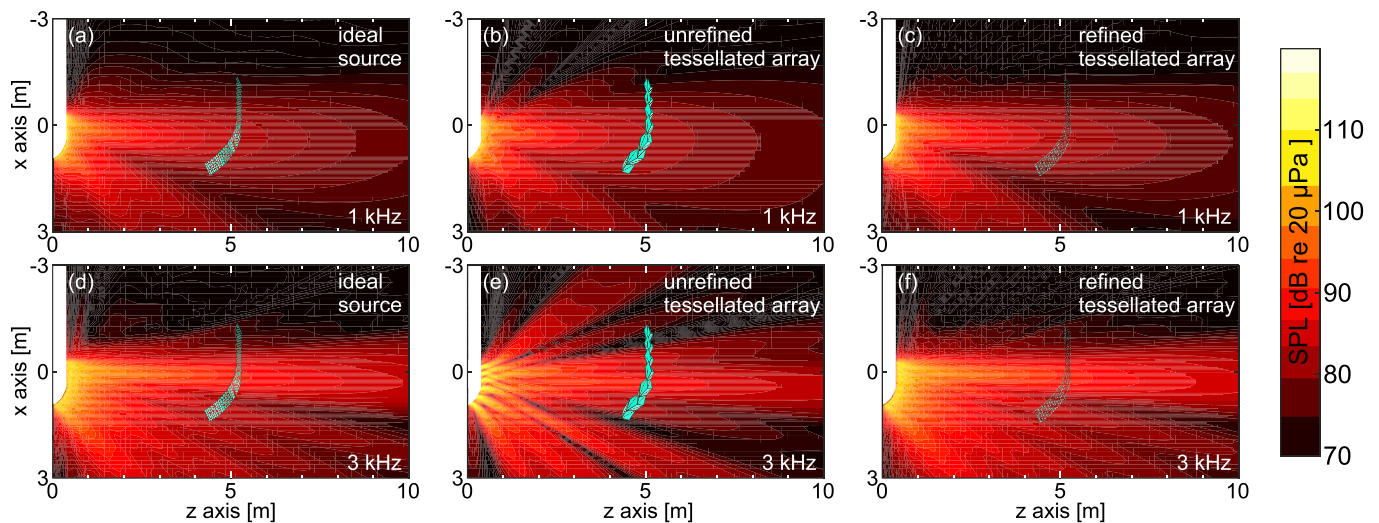


FIG. 4. (Color online) SPL in the $x-z$ plane. The SPL of the ideal source [(a),(d)], unrefined tessellated array [(b),(e)], and refined tessellated array [(c),(f)] are, respectively, shown at 1 kHz (top row) and 3 kHz (bottom row). The unshaded areas are shown where the sources lay.

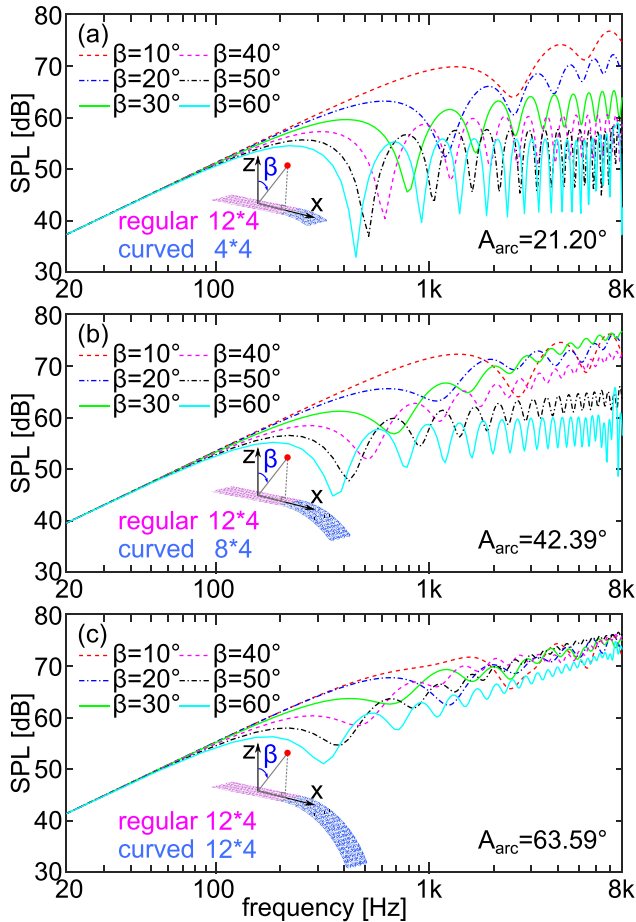


FIG. 5. (Color online) SPL of piecewise tessellated acoustic sources as a function of driving frequency. Each plot includes the results for six different elevation angles for azimuth angle $\phi = 0^\circ$. The acoustic sources are refined tessellation with the same tessellated sub-array of regular Miura-ori (12×4), but the sub-arrays of curved Miura-ori are 4×4 (a), 8×4 (b), and 12×4 (c), respectively. The considered elevation angles are 10° , 20° , 30° , 40° , 50° , and 60° . Driving frequency and radial distance are 5 kHz and 20 m, respectively.

Considering the piecewise assembled array in Fig. 5(a), it is seen that the array radiates acoustic waves in a manner similar to a monopole in the frequency range around [20,150] Hz. In other words, the acoustic pressure amplitude is linearly proportional with the driving frequency, so that the SPL changes linearly for logarithmic frequency change. With the increase of frequency, i.e., wavenumber, the phase difference between acoustic waves radiated from different parts of the piecewise array becomes greater than 180° . This means that the particle velocity of waves radiated from different ends of the array may destructively interfere, as evidenced by nodes of SPL seen at frequencies around 400 Hz and greater. Considering $\beta = 60^\circ$ in Fig. 5(a) for instance, the SPL fluctuation is around 21 dB. On the other hand, for the field point at $\beta = 10^\circ$ the fluctuation of SPL is less than about 10 dB. In Fig. 5(b), an additional 4×4 sub-array of curved Miura-ori oscillating facets is added so that the curved arc length encompasses an angle of $A_{\text{arc}} = 42.39^\circ$. As a result, the fluctuation of SPL at $\beta = 60^\circ$ is reduced so that the greatest ripple of SPL is around 15 dB. To further increase the angular range of uniform response, another

4×4 sub-array of curved Miura-ori is assembled for the results shown in Fig. 5(c). As a result, the fluctuation of SPL at $\beta = 60^\circ$ is further reduced. These examples reveal that the assembly of standardized modules into tessellated acoustic arrays empowers means to obtain desired spectral uniformity in the far field. Due to the low-dimensional foldability of Miura-ori,¹⁴ the findings of Fig. 5 are extensible to a broad range of linear and curved conformations of piecewise assembled arrays via folding. Such versatility may not have an equivalent for conventional, ideal sources with fixed shapes.

IV. EXPERIMENTAL VALIDATION AND ASSESSMENT

To test the efficacy of the characteristics of the piecewise, tessellated acoustic arrays, a proof-of-concept specimen is fabricated and the experimental results are reported in this section.

A. Proof-of-concept specimen design and fabrication

The specimen shown in Fig. 6(a) is assembled from a 3×1 unit cell sub-array of regular Miura-ori and a 3×1 unit cell sub-array of curved Miura-ori. The facet dimensions are $a_1 = 0.048$ m, $b_1 = 0.06$ m, $\gamma_1 = 60^\circ$, and $\gamma_2 = 40^\circ$. The facets are made of corrugated polypropylene with square cross-section corrugations. The thickness of the corrugated material is 5 mm, the pitch is two sheets per cm, and the thickness of the polypropylene sheet is 0.3 mm. Each facet is itself an assembly of four sub-facets that are cut into shapes by a laser cutter (Full Spectrum Laser, Las Vegas, NV) in a way such that the edges of each sub-facet terminate in a flute of the corrugated polypropylene. Once the sub-facets are

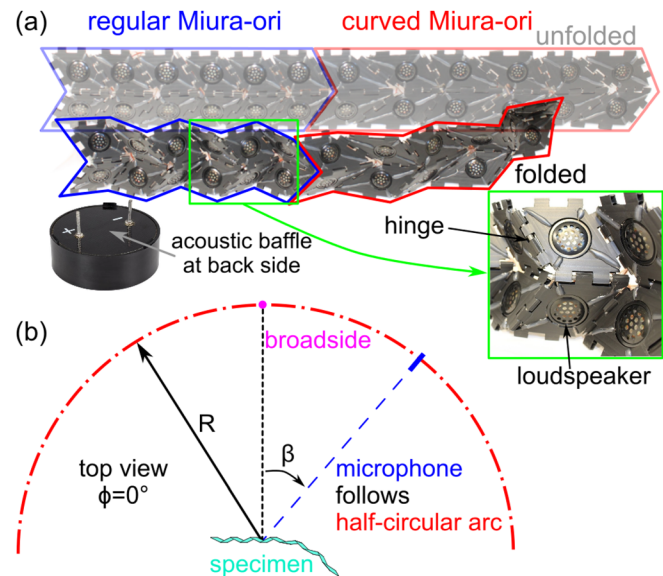


FIG. 6. (Color online) Overview of the specimen and experimental setup. (a) The piecewise specimen is assembled from three regular Miura-ori and three curved Miura-ori unit cell sub-arrays with centrally mounted loudspeakers. The close-up picture shows the kinematic hinge and loudspeaker. The inset illustrates the acoustic baffle at the back side of the loudspeaker. (b) Top view schematic to demonstrate the experimental setup to measure SPL as a function of the elevation angle β in a hemi-anechoic acoustic chamber, where the microphone follows a half circle with radius $R \approx 3$ m.

assembled into a facet, a miniature loudspeaker (Parts Express, Springboro, OH) is bonded at the center of the facet. As shown in the inset of Fig. 6(a), each loudspeaker is individually baffled at the back side. Threaded rods are inserted into the fluted edges of adjacent facets to create kinematic hinges in agreement with the analytical formulation assumptions.

B. Experimental setup

Measurements are undertaken inside a hemi-anechoic acoustic chamber of interior usable volumetric dimensions $7.78\text{ m} \times 10.9\text{ m} \times 4.66\text{ m}$. A microphone (PCB Piezotronics, Depew, NY, 130E20) at a radial distance $R \approx 3\text{ m}$ follows a half circle in the plane $\phi = 0^\circ$ to measure the acoustic pressure, as shown in Fig. 6(b). The elevation angle is recorded by a rotary encoder (Signswise). Each measurement is taken with a single frequency signal sent to an audio amplifier (Pyle, Brooklyn, NY, PFA330). The amplified signal drives all the loudspeakers in unison by parallel connections. Acquired microphone and rotary encoder data are post-processed in MATLAB (MathWorks, Natick, MA) through a data acquisition system (National Instruments, Austin, TX, USB-6341).

C. Comparison of experimental and analytical results

In the analytical model developed in Sec. II, the full facet area is assumed to oscillate and thus radiate acoustic waves into the adjacent fluid. Yet, the proof-of-concept specimen utilizes circular loudspeaker transducers positioned at the center of each facet. In this way, only a portion of the facet area radiates acoustic waves. To improve the efficacy of the comparison between model results and experimental data, here the analysis is extended to consider the exact experimental conditions. Namely, a circular piston around the geometric center of facet is assumed to radiate waves. This ‘‘circular piston approximation’’ of the original analytical derivation is then contrasted to the experimental

measurements of SPL in Fig. 7. For the top and bottom rows of Fig. 7, the folding angles θ are 0° and 10° , respectively. The driving frequencies considered are 2 kHz in Figs. 7(a) and 7(d), 4 kHz in Figs. 7(b) and 7(e), and 7 kHz in Figs. 7(c) and 7(f). The normal velocity amplitude u_0 used in the analysis is determined empirically to be 0.03 m/s.

Considering 2 kHz in Fig. 7(a) for the unfolded configuration of the array, three nodes are predicted and measured for both sides of the array constituting regular and curved Miura-ori sub-arrays. An asymmetric SPL distribution is shown for this unfolded state of the array, due to the asymmetric placement of the loudspeakers considering the distinct folding patterns of regular and curved Miura-ori. This asymmetry is quantitatively realized by both experimental measurements and the circular piston approximation in Fig. 7(a). For 4 kHz in Fig. 7(b), the SPL values are greater toward the broadside $\beta = 0^\circ$ while an increasing number of sidelobes are found in both analysis and experiment. When the frequency is further increased to 7 kHz in Fig. 7(c), two grating lobes appear in experiments, which are also predicted by the circular piston analytical approximation. The bottom row of Fig. 7 presents the results at the same 1, 4, and 7 kHz frequencies with the array folded to $\theta = 10^\circ$. For both Fig. 7(d) at 1 kHz and 4 kHz in Fig. 7(e), the SPL radiated from the curved Miura-ori side of the array is more uniform than from the unfolded array in Figs. 7(a) and 7(b), exemplifying the contribution of the curved segment for the folded array. For example, the SPL difference between $\beta = 0^\circ$ and 90° on the right side of Fig. 7(a) is around 40 dB, while the value is decreased to around 20 dB in Fig. 7(d). The grating lobes observed at 7 kHz in Fig. 7(c) are also suppressed for the folded array in Fig. 7(f). The discrepancies between analysis and experiments may come from reflected and diffracted waves that are not accounted for in the analysis. The deviations may also result from variability inherent in the experimental setup. For example, the folded array configuration may deviate from the ideal conformation for a known angle of folding. Despite these slight discrepancies, the results

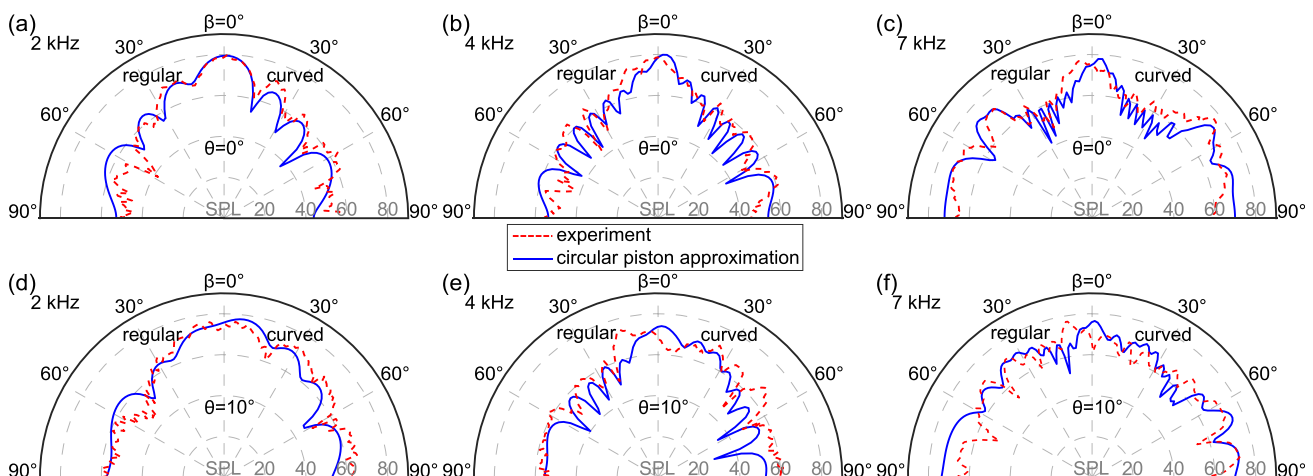


FIG. 7. (Color online) SPL as a function of the elevation angle β of field point at azimuth angle $\phi = 0^\circ$. Each plot includes the experimental (dashed red) and circular piston analytical (solid blue) results. The orientation of the specimen is the same as Fig. 6(b), and consequently the left and right of each sub-figure correspond to regular and curved Miura-ori sub-arrays, respectively. The driving frequencies are 2 kHz [(a),(d)], 4 kHz [(b),(e)], and 7 kHz [(c),(f)], respectively. The folding angles θ are 0° (top row) and 10° (bottom row), respectively.

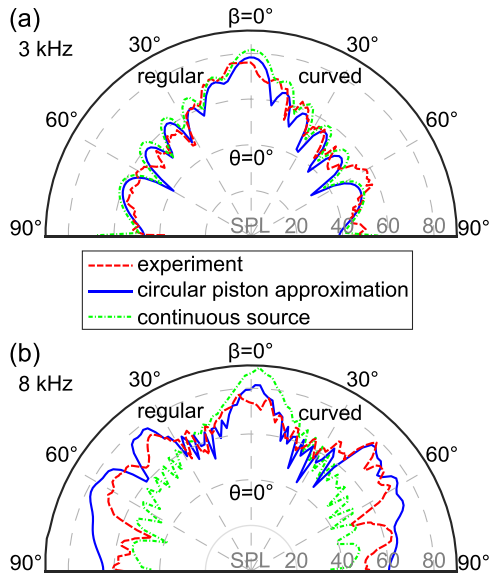


FIG. 8. (Color online) SPL as a function of elevation angle β of field point at azimuth angle $\phi = 0^\circ$. Each plot includes the experimental (dashed red), circular piston analysis (solid blue), and continuous array analysis (dotted-dashed green) results. The orientation of the specimen is the same as Fig. 6(b), and consequently the left and right of each sub-figure correspond to regular and curved Miura-ori sub-arrays, respectively. The driving frequencies are 3 kHz (a) and 8 kHz (b), respectively, and the tessellation is unfolded ($\theta = 0^\circ$).

reveal that the principle of combining regular and curved Miura-ori modules to the piecewise tessellated array permits the folded system to manipulate the relative uniformity of far field SPL.

To quantify the differences between the original analytical model that presumes the whole area of the facets radiate acoustic waves (here termed “continuous array” prediction) when compared to the circular piston approximation, the respective analytical predictions are compared in Fig. 8 against the experimental data. The frequencies are 3 kHz and 8 kHz in Figs. 8(a) and 8(b), respectively, considering the unfolded configuration of the array $\theta = 0^\circ$.

For 3 kHz in Fig. 8(a), it is seen that predictions by the continuous array and circular piston approximation analyses are in good agreement, despite magnitude deviations associated with different total radiating surface areas. These results also agree well with the experimental data. When the frequency is increased to 8 kHz in Fig. 8(b), grating lobes are predicted by the circular piston approximation and are also observed in the measurements. Yet, these grating lobes are not predicted in the continuous array analysis. The spacing between transducer elements in an array of circular pistons permits constructive interference at other field points in addition to the broadside. Yet, the continuous array does not cause such grating lobe phenomena.⁷ Considering the experimental system dimensions, the grating lobes are manifest for the tessellated array when the wavelength is on the order of the facet diagonal dimension. For lower frequencies, such as in the case of 3 kHz examined in Fig. 8(a) where the wavelength spans multiple facets, the analytical model established in this research is viable to accurately characterize the roles of folding, modularity, and system design on the adaptive

acoustic energy delivery from the piecewise, tessellated acoustic arrays.

V. CONCLUSIONS

This work investigates the acoustic characteristics of piecewise assembled acoustic arrays formed upon reconfigurable tessellated structures. The foldability and modularity of the origami-inspired architectures are found to lend great versatility to adapt the distribution and spectral features of the radiated acoustic fields. Analytical studies demonstrate that the piecewise array may emulate the acoustic wave radiation of an ideal J-shaped acoustic source, while the tessellation may need refinement depending on the acoustic wavelength with respect to facet dimensions. The modeling approach established here may be extended to other piecewise assembled tessellated arrays. Considering the vastness of available origami tessellations programmability of folding patterns, numerous reconfigurable array topologies may be scrutinized by the analysis presented here. Furthermore, the study of modularity in this work exemplifies that the periodicity of origami-inspired structures facilitates beneficial standardization of array fabrication and assembly for practical applications.

ACKNOWLEDGMENTS

This work is supported by the National Science Foundation Faculty Early Career Development Award (No. 1749699).

APPENDIX

The spatial extents of the folded unit cell of regular Miura-ori are derived by Schenk and Guest.²⁹ For completeness of the derivation in Sec. II, the expressions are repeated here:

$$H = a \sin \theta \sin \gamma, \quad (\text{A1a})$$

$$S = b \frac{\cos \theta \tan \gamma}{\sqrt{1 + \cos^2 \theta \tan^2 \gamma}}, \quad (\text{A1b})$$

$$L = a \sqrt{1 - \sin^2 \theta \sin^2 \gamma}, \quad (\text{A1c})$$

$$V = b \frac{1}{\sqrt{1 + \cos^2 \theta \tan^2 \gamma}}. \quad (\text{A1d})$$

¹K. Fuchi, J. Tang, B. Crowgey, A. R. Diaz, E. J. Rothwell, and R. O. Ouedraogo, “Origami tunable frequency selective surfaces,” *IEEE Antennas Wireless Propag. Lett.* **11**, 473–475 (2012).

²S. Bildik, S. Dieter, C. Fritzsche, W. Menzel, and R. Jakoby, “Reconfigurable folded reflectarray antenna based upon liquid crystal technology,” *IEEE Trans. Antennas Propag.* **63**, 122–132 (2015).

³S. Babaei, J. T. B. Overvelde, E. R. Chen, V. Tourmat, and K. Bertoldi, “Reconfigurable origami-inspired acoustic waveguides,” *Sci. Adv.* **2**, e1601019 (2016).

⁴M. Thota, S. Li, and K. W. Wang, “Lattice reconfiguration and phononic band-gap adaptation via origami folding,” *Phys. Rev. B* **95**, 064307 (2017).

- ⁵K. Zhang, Y. H. Jung, S. Mikael, J. H. Seo, M. Kim, H. Mi, H. Zhou, Z. Xia, W. Zhou, S. Gong, and Z. Ma, "Origami silicon optoelectronics for hemispherical electronic eye systems," *Nat. Commun.* **8**, 1782 (2017).
- ⁶T. Wu, S. S. Hamann, A. C. Ceballos, C. E. Chang, O. Solgaard, and R. T. Howe, "Design and fabrication of silicon-tessellated structures for mono-centric imagers," *Microsyst. Nanoeng.* **2**, 16019 (2016).
- ⁷L. E. Kinsler, A. R. Frey, A. B. Coppens, and J. V. Sanders, *Fundamentals of Acoustics* (Wiley, New York, 2000).
- ⁸J. Benesty and J. Chen, *Study and Design of Differential Microphone Arrays* (Springer, Berlin, 2013).
- ⁹B. D. Van Veen and K. M. Buckley, "Beamforming: A versatile approach to spatial filtering," *IEEE ASSP Mag.* **5**, 4–24 (1988).
- ¹⁰B. D. Steinberg, *Principles of Aperture and Array System Design: Including Random and Adaptive Arrays* (Wiley, New York, 1976).
- ¹¹F. A. Jolesz and K. H. Hynynen, *MRI-Guided Focused Ultrasound Surgery* (CRC Press, New York, 2007).
- ¹²L. Azar, Y. Shi, and S. C. Wooh, "Beam focusing behavior of linear phased arrays," *NDT&E Int.* **33**, 189–198 (2000).
- ¹³I. F. Akyildiz, D. Pompili, and T. Melodia, "Underwater acoustic sensor networks: Research challenges," *Ad Hoc Networks* **3**, 257–279 (2005).
- ¹⁴R. L. Harne and D. T. Lynd, "Origami acoustics: Using principles of folding structural acoustics for simple and large focusing of sound energy," *Smart Mater. Struct.* **25**, 085031 (2016).
- ¹⁵C. Zou and R. L. Harne, "Adaptive acoustic energy delivery to near and far fields using foldable, tessellated star transducers," *Smart Mater. Struct.* **26**, 055021 (2017).
- ¹⁶C. Zou, D. T. Lynd, and R. L. Harne, "Acoustic wave guiding by reconfigurable tessellated arrays," *Phys. Rev. Appl.* **9**, 014009 (2018).
- ¹⁷S. A. Zirbel, R. J. Lang, M. W. Thomson, D. A. Sigel, P. E. Walkemeyer, B. P. Trease, S. P. Magleby, and L. L. Howell, "Accommodating thickness in origami-based deployable arrays," *J. Mech. Des.* **135**, 111005 (2013).
- ¹⁸T. U. Lee and J. M. Gattas, "Geometric design and construction of structurally stabilized accordion shelters," *J. Mech. Rob.* **8**, 031009 (2016).
- ¹⁹S. A. Glegg, M. P. Olivieri, R. K. Coulson, and S. M. Smith, "A passive sonar system based on an autonomous underwater vehicle," *IEEE J. Ocean. Eng.* **26**, 700–710 (2001).
- ²⁰R. Fisher, K. Thomenius, R. Wodnicki, R. Thomas, S. Cogan, C. Hazard, W. Lee, D. Mills, B. Khuri-Yakub, A. Ergun, and G. Yaralioglu, "Reconfigurable arrays for portable ultrasound," in *Proceedings of IEEE Ultrasonics Symposium*, Rotterdam (2005), pp. 495–499.
- ²¹W. Li, D. Torres, R. Díaz, Z. Wang, C. Wu, C. Wang, Z. L. Wang, and N. Sepúlveda, "Nanogenerator-based dual-functional and self-powered thin patch loudspeaker or microphone for flexible electronics," *Nat. Commun.* **8**, 15310 (2017).
- ²²T. Tachi, "Freeform variations of origami," *J. Geom. Graphics* **14**, 203–215 (2010).
- ²³L. H. Dudte, E. Vouga, T. Tachi, and L. Mahadevan, "Programming curvature using origami tessellations," *Nat. Mater.* **15**, 583–588 (2016).
- ²⁴R. E. Christiansen and E. Fernandez-Grande, "Design of passive directional acoustic devices using topology optimization—from method to experimental validation," *J. Acoust. Soc. Am.* **140**, 3862–3873 (2016).
- ²⁵M. S. Ureda, "Analysis of loudspeaker line arrays," *J. Audio Eng. Soc.* **52**, 467–795 (2004).
- ²⁶D. B. Keele, Jr., "A performance ranking of seven different types of loudspeaker line arrays," in *Audio Engineering Society Convention* (2010), San Francisco, p. 129.
- ²⁷J. M. Gattas, W. Wu, and Z. You, "Miura-base rigid origami: Parameterizations of first-level derivative and piecewise geometries," *J. Mech. Des.* **135**, 111011 (2013).
- ²⁸J. M. Gattas and Z. You, "Geometric assembly of rigid-foldable morphing sandwich structures," *Eng. Struct.* **94**, 149–159 (2015).
- ²⁹M. Schenk and S. D. Guest, "Geometry of Miura-folded metamaterials," *Proc. Natl. Acad. Sci. U.S.A.* **110**, 3276–3281 (2013).
- ³⁰K. B. Ocheltree and L. A. Frizzell, "Sound field calculation for rectangular sources," *IEEE Trans. Ultrason., Ferroelectr. Freq. Control* **36**, 242–248 (1989).
- ³¹I. Wolff and L. Malter, "Directional radiation of sound," *J. Acoust. Soc. Am.* **2**, 201–241 (1930).